AIAA 94-0462

A Navier-Stokes/Kirchhoff Method For Noise Radiation From Ducted Fans

Yusuf Ozyoruk and Lyle N. Long
The Pennsylvania State University
University Park, PA

32nd Aerospace Sciences Meeting & Exhibit
January 10-13, 1994 / Reno, NV

AIAA-94-0462

A NAVIER-STOKES/KIRCHHOFF METHOD FOR NOISE RADIATION FROM DUCTED FANS

Yusuf Özyörük* and Lyle N. Long†
Aerospace Engineering Department
The Pennsylvania State University, University Park, PA 16802

Abstract

Nonlinear acoustic effects associated with high speed flow, engine liners, and sound propagation through (possibly turbulent) boundary layers make the prediction of noise radiation from advanced ducted fans a very difficult problem. This paper discusses a numerical algorithm being developed to solve this highly complicated problem on a massively parallel Connection Machine computer. These computers currently have a peak speed of 131 billion operations per second and in the near future will be capable of over a trillion operations per second, which will allow us to predict aeroacoustics more accurately than previously possible. The scheme that has been implemented is a hybrid scheme that solves the 3-D Navier-Stokes equations in the near-field and then uses a moving Kirchhoff surface to predict the far-field. The Navier-Stokes equations are solved in a time-accurate manner using a finite volume scheme and Runge-Kutta time marching. The resulting solution from this is then passed to the Kirchhoff surface routine, based on the theory of Farassat and Myers [5]. The Kirchhoff method is shown to work very well with a moving monopole test case. Nonreflecting boundary conditions are important in computational aeroacoustics, and these conditions of the Navier-Stokes algorithm are also shown to work well. The coupling of the Navier-Stokes and Kirchhoff methods is described and some test results are presented. Preliminary results show that the schemes are able to effectively use the massively parallel computers.

1 Introduction

Computational fluid dynamics techniques and computational aeroacoustics techniques have become more and more similar over the last few years. This is due to two effects: 1) faster computers allow us to simulate more of the physics of the flow and 2) as we investigate more complicated aeroacoustic phenomena we must simultaneously solve the fluid dynamics and the aeroacoustics due to the coupling between them. Noise radiation from high bypass ratio advanced ducted fans forms one of the most complicated aeroacoustic problems. Nonlinear acoustic effects associated with high speed flow, engine liners, and sound propagation through (possibly turbulent) boundary layers make the prediction of noise radiation from ducted fans a very difficult task.

Noise radiated forward from a high bypass ratio engine is mostly generated by the fan. Due to high tip speeds of the blades of the fan, there is usually a shock wave pattern that radiates into the duct of the engine inlet [1] in addition to the rotor-stator interaction tones [2]. Considering that there is also a high speed sheared mean flow in an engine inlet duct, the complexity of the problem becomes apparent. Analysis of sound radiation from ducted fans has been mostly limited to linear theory [1], [3]. However, a more complete theory is required to analyze sound propagation and radiation in high bypass ratio ducted fans due to nonlinearity involved. This research is not concerned with sound generating mechanisms at the fan, but is concerned with sound propagation through nonuniform engine inlets and radiation to free space. Therefore, the Navier-Stokes equations will be solved throughout the engine inlet and in the close surroundings with a given sound source or a simple model at the fan stage.

In computational aeroacoustic (CAA) calculations that use standard finite difference or finite volume methods in 3-D space, one may not be able to use a computational domain that extends to the point of interest. This is due to both computational speed and memory limitations and possible phase and amplitude errors that can accumulate. Therefore, one usually truncates the computational domain using nonreflecting boundary conditions on the artificial boundary. One can then use the Kirchhoff method that has recently been used [4] to predict far-field sound radiation from moving surfaces. This method can be effectively used provided that the time-history of the acoustic pressure on such a surface is known [5].

*Graduate Research Assistant
†Assistant Professor, Senior Member, AIAA

Even though there has been great progress in the development of radiation boundary conditions [6], [7], reflections from the artificial boundaries may still occur. The accuracy near these boundaries may not be as high as at interior points. To minimize these effects, one can also construct a Kirchhoff surface in the interior of a computational domain and use this surface to predict the far-field noise level. This would provide a buffer region between the Kirchhoff surface and the far-field and may permit one to use the natural damping of larger cells to minimize unwanted reflections back into the domain (since no far-field boundary condition is truly non-reflecting at this time).

The Navier-Stokes algorithm is described in the following section, which is followed by a discussion of the Kirchhoff method. Results of some steady and unsteady flow problems are presented and a description of the coupling of the Navier-Stokes method with the Kirchhoff method is given along with some test results.

2 Navier-Stokes Algorithm

This section describes the 3-D Navier-Stokes part of the hybrid scheme. The integral form of the Navier-Stokes equations are solved using finite volume discretization through a four-stage Runge-Kutta time marching technique. The form of the Navier-Stokes equations being solved is given by

$$\frac{\partial}{\partial t}\int\int\int_V \begin{bmatrix} \rho \\ \rho\vec{V} \\ \rho E \end{bmatrix} dV \qquad (1)$$

$$+\int\int_S \begin{bmatrix} \rho\vec{V}\cdot\hat{n} \\ \rho\vec{V}(\vec{V}\cdot\hat{n}) - \hat{n}\cdot\overline{\overline{\sigma}} \\ (\rho E + p)\vec{V}\cdot\hat{n} - \hat{n}\cdot\overline{\overline{\tau}}\cdot\vec{V} + \vec{q}\cdot\hat{n} \end{bmatrix} dS = 0$$

where ρ, $\vec{V}$, ρE, $\overline{\overline{\sigma}}$, $\overline{\overline{\tau}}$, $\vec{q}$, and $\hat{n}$ are the density, velocity, total energy, total stress tensor, shear stress tensor, heat flux, and the unit normal vector on the surface, respectively. For a perfect gas the total energy is given as $\rho E = p/(\gamma-1) + \frac{1}{2}\rho\vec{V}\cdot\vec{V}$. The shear stress is given as $\tau_{ij} = \mu[(\partial u_i/\partial x_j + \partial u_j/\partial x_i) - \frac{2}{3}\delta_{ij}\nabla\cdot\vec{V}]$, where δ_{ij} is the Kronecker delta function. The stress tensor is related to the pressure and the shear stress tensor by $\sigma_{ij} = -p\delta_{ij} + \tau_{ij}$. The heat flux $\vec{q}$ is given by the Fourier law, $\vec{q} = -k\nabla T$, T being the temperature. With the divergence theorem, Equation (1) can also be written as

$$\int\int\int_V \vec{Q}\, dV + \int\int\int_V \nabla\cdot\vec{F}\, dV = 0. \qquad (2)$$

Without the integral signs this is the conservative form of the Navier-Stokes equations used in finite differencing. The numerical integration of these equations starts with decomposition of the computational domain into small hexahedral cells (structured grid). When transformed in the curvilinear coordinate system and applied to a computational cell (i,j,k), shown in Figure 1, the above equations take the following form:

$$\frac{d}{dt}(\Delta V\bar{Q})_{i,j,k} + (E^*_{i+1/2,j,k} - E^*_{i-1/2,j,k}) + (F^*_{i,j+1/2,k} - F^*_{i,j-1/2,k}) + (G^*_{i,j,k+1/2} - G^*_{i,j,k-1/2}) = 0 \qquad (3)$$

where ΔV is the cell volume and $\bar{Q}$ is the cell averaged value of Q:

$$\Delta V\ \bar{Q}^* = \int\int\int_V \frac{Q}{J}\, d\xi\, d\eta\, d\zeta, \qquad (4a)$$

and

$$E^* = \int\int_{\Omega_\xi} \frac{1}{J}(\xi_x E + \xi_y F + \xi_z G)\, d\eta\, d\zeta, \qquad (4b)$$

$$F^* = \int\int_{\Omega_\eta} \frac{1}{J}(\eta_x E + \eta_y F + \eta_z G)\, d\xi\, d\zeta, \qquad (4c)$$

$$G^* = \int\int_{\Omega_\zeta} \frac{1}{J}(\zeta_x E + \zeta_y F + \zeta_z G)\, d\xi\, d\eta \qquad (4d)$$

where E, F, and G are the components of the flux-vector tensor $\vec{F}$ that appears in Equation 2. The Jacobian and the metrics are related to the volume of the integration element and its surface vector by

$$dV = \frac{1}{J}\, d\xi\, d\eta\, d\zeta,$$

$$n^\xi_x dS = \frac{\xi_x}{J} d\eta\, d\zeta,\ n^\xi_y dS = \frac{\xi_y}{J} d\eta\, d\zeta,\ n^\xi_z dS = \frac{\xi_z}{J} d\eta\, d\zeta,$$

$$n^\eta_x dS = \frac{\eta_x}{J} d\xi\, d\zeta,\ n^\eta_y dS = \frac{\eta_y}{J} d\xi\, d\zeta,\ n^\eta_z dS = \frac{\eta_z}{J} d\xi\, d\zeta,$$

$$n^\zeta_x dS = \frac{\zeta_x}{J} d\xi\, d\eta,\ n^\zeta_y dS = \frac{\zeta_y}{J} d\xi\, d\eta,\ n^\zeta_z dS = \frac{\zeta_z}{J} d\xi\, d\eta$$

where an n with a superscript ξ and a subscript x indicates the x-component of the normal vector on the constant ξ-surface in the curvilinear coordinate system.

The velocity and temperature gradients that appear in the stress tensor $\overline{\overline{\tau}}$ and the heat flux $\vec{q}$, respectively, can be obtained using Gauss' divergence theorem. In the cartesian system

$$\int\int\int_V \frac{\partial u_i}{\partial x_j}\, dV = \int\int_S u_i n_j\, dS.$$

The cell average of the derivative of u_i with respect to x_j is then approximated by

$$\overline{\frac{\partial u_i}{\partial x_j}} = \frac{1}{\Delta V}\int\int\int_V u_i n_j\, dS.$$

2.1 Runge-Kutta time integration

Equations (3) are integrated using a fourth order accurate *four-stage Runge-Kutta time marching technique*. The stages of this integration technique are given as

$$\bar{Q}^{(1)} = \bar{Q}^n$$

$$\bar{Q}^{(p)} = \bar{Q}^n - \alpha_{p-1}\frac{\Delta t}{\Delta V}[F(Q^{(p-1)})] - D(Q^{(p-1)})],$$

$$\bar{Q}^{n+1} = \bar{Q}^n - \frac{\Delta t}{\Delta V}\sum_{p=1}^{4}\beta_p[F(Q^{(p)})] - D(Q^{(p)})] \quad (5)$$

where the superscript n refers to the nth time step, and F and D are the total fluxes, D being the artificial dissipation flux. The constants α and β are given by

$$\alpha = [1/2, 1/2, 1], \ \beta = [1/6, 1/3, 1/3, 1/6].$$

2.2 Second order accurate finite volume discretization:

Cartesian flux components E, F, and G of the flux-vector tensor $\vec{F}$ are functions of the dependent flow variables $Q = [\rho, \rho\vec{V}, \rho E]^T$. Therefore, evaluation of the surface integrals requires these quantities on the cell faces, along with the metrics. The usual approach for a second order accurate finite volume discretization is first to calculate the components E, F, and G at the cell centers and then take the average of two neighboring cells to determine these values at their common face [8], [9], [10]. A subsequent assumption of constant flux over a face and an integration over all the faces of each cell result in a second order accurate scheme on sufficiently smooth grids. Due to resemblance of this approach to central differencing, the scheme must be augmented with artificial dissipation to prevent odd-even decoupling. A blend of second and fourth order dissipation of Jameson *et al.* [10] is used.

2.3 Fourth order accurate finite volume discretization:

In the second order finite volume discretization, taking the average flux of two neighboring cells to determine the flux at their common face and an integration with constant flux assumption on the face were sufficient for a second order accuracy. However, for higher order accurate schemes higher order surface integrations are necessary. For this reason the dependent variables Q are allowed to vary on the cell faces. The surface integrals (4b,c,d) are then computed with a Gaussian quadrature technique, which is widely used in integral based methods such as finite element and boundary element.

The method chosen here to calculate the surface integrals of the 3-D Navier-Stokes equations is similar to that of Rai and Chakravarty [11], who solved the conservative form of the 2-D Euler equations using an implicit upwind method. They started with a finite difference grid and constructed a control volume around each grid point to integrate the equations. They determined the flow quantities at the Gaussian points using interpolations, and obtained the pointwise values of the integrated solution using the reconstruction via a deconvolution technique, which is described in Refs. [11], [12], and also briefly described later in this section.

The surface flux integrations are performed using 2-point Gaussian quadrature in each direction. The dependent variables Q at Gaussian points on a cell face are determined by interpolations in the computational domain. For example, at the Gaussian point $(i+1/2, j+j_g, k+k_g)$ on a constant ξ-face, see Figure 2, any dependent variable Q is determined with three successive interpolation operations which are given as

$$\begin{aligned} Q_{i+1/2,j+j_g,k+k_g} &= \sum_{q=-2}^{2} a_q(k_g) \sum_{p=-2}^{2} a_p(j_g) Q_{i+1/2,j+p,k+q} \\ &= \sum_{p=-2}^{2} a_p(j_g) \sum_{q=-2}^{2} a_q(k_g) Q_{i+1/2,j+p,k+q} \\ &= \sum_{p=-2}^{2} a_p(j_g) \sum_{q=-2}^{2} a_q(k_g) \sum_{r=-2}^{3} c_r Q_{i+r,j+p,k+q} \end{aligned}$$

where the constants c_r are given by

$$c_r = \frac{1}{3840}\{45, -375, 2250, 2250, -375, 45\}$$

and the interpolation functions a are given by

$$\begin{aligned} a_{-2}(\phi) &= \frac{1}{24}(2\phi - \phi^2 - 2\phi^3 + \phi^4), \\ a_{-1}(\phi) &= \frac{1}{24}(-16\phi + 16\phi^2 + 4\phi^3 - 4\phi^4), \\ a_0(\phi) &= \frac{1}{24}(24 - 30\phi^2 + 6\phi^4), \\ a_{+1}(\phi) &= \frac{1}{24}(16\phi + 16\phi^2 - 4\phi^3 - 4\phi^4), \\ a_{+2}(\phi) &= \frac{1}{24}(-2\phi - \phi^2 + 2\phi^3 + \phi^4). \end{aligned}$$

The above coefficients c_r and the functions a are given for interior points and special biased interpolations are used near the boundaries. The cells and the cell faces that are involved in these interpolation operations are illustrated in Figure 3. The interpolation in the i-direction is fifth order accurate and in the other directions it is fourth order accurate. The procedure for

finding Q at the other cell faces are defined similarly. The components E, F, and G at a Gaussian point are then

$$E_{i+1/2,j+j_g,k+k_g} = E(Q_{i+1/2,j+j_g,k+k_g})$$

$$F_{i+1/2,j+j_g,k+k_g} = F(Q_{i+1/2,j+j_g,k+k_g})$$

$$G_{i+1/2,j+j_g,k+k_g} = G(Q_{i+1/2,j+j_g,k+k_g}).$$

The metrics at the Gaussian points must also be computed using a higher order accurate scheme. A secondary finer grid is constructed such that the new grid lines split each cell face into 16 quadrilateral's (see Figure 1). The grid points of the finer mesh are obtained from the original grid via interpolations. Then the metrics can be calculated at the Gaussian points using piecewise interpolation polynomials. In second order finite volume techniques a cell face is assumed to be planar. This may cause nonconservative integrations in complex geometries where a cell face may not be planar. This difficulty is somewhat removed in the higher order finite volume method by higher order approximations of the metrics.

Since the total fluxes of the Runge-Kutta integration, Equation (5), are functions of the pointwise dependent variables Q, and the solution variables $\bar{Q}$ is the cell averaged quantities, a reconstruction of the solution from the averaged quantities is necessary. The reconstruction is achieved by a deconvolution procedure [11], [12]. A moving average of any variable w in the three dimensional computational domain is defined as

$$\bar{w}(\xi,\eta,\zeta)$$

$$= \frac{1}{h^3}\int\int\int_{-h/2}^{h/2} w(\xi+\xi',\eta+\eta',\zeta+\zeta')\,d\xi'\,d\eta'\,d\zeta'.$$

A Taylor series expansion is performed about $\xi' = 0, \eta' = 0, \zeta' = 0$ and then the integration is performed:

$$\bar{w}(\xi,\eta,\zeta) = w(\xi,\eta,\zeta)$$

$$+\frac{h^2}{24}\left(\frac{\partial^2}{\partial\xi^2}+\frac{\partial^2}{\partial\eta^2}+\frac{\partial^2}{\partial\zeta^2}\right)w(\xi,\eta,\zeta)+O(h^4) \quad (6)$$

From this equation one can obtain, by differentiation, the following relations:

$$h^2\frac{\partial^2\bar{w}}{\partial\xi^2} = h^2\frac{\partial^2 w}{\partial\xi^2}+O(h^4),$$

$$h^2\frac{\partial^2\bar{w}}{\partial\eta^2} = h^2\frac{\partial^2 w}{\partial\eta^2}+O(h^4),$$

$$h^2\frac{\partial^2\bar{w}}{\partial\zeta^2} = h^2\frac{\partial^2 w}{\partial\zeta^2}+O(h^4).$$

By substitution of these terms into Equation (6) we have the pointwise quantity $w(\xi,\eta,\zeta)$ as

$$w(\xi,\eta,\zeta) = \bar{w}(\xi,\eta,\zeta)$$

$$-\frac{h^2}{24}\left(\frac{\partial^2}{\partial\xi^2}+\frac{\partial^2}{\partial\eta^2}+\frac{\partial^2}{\partial\zeta^2}\right)\bar{w}(\xi,\eta,\zeta)+O(h^4)$$

where $h = \Delta\xi = \Delta\eta = \Delta\zeta$. Thus the total fluxes $F(Q)$ of Equation (5) are corrected for the fourth order accuracy adding $-\frac{h^2}{24}(F_{\xi\xi}(Q)+F_{\eta\eta}(Q)+F_{\zeta\zeta}(Q))$ to it. The second order derivative terms are computed using a second order accurate finite differencing since these terms are in multiplication with h^2.

2.4 Boundary Conditions:

The current CFD method uses two different sets of far-field boundary conditions. One set uses the locally one dimensional Riemann invariants based characteristic boundary conditions, which are usually used in steady state flow calculations. For time accurate problems one should use time accurate boundary conditions.

The Riemann invariants for incoming and outgoing waves are given by

$$R_\infty = V_{n_\infty} - \frac{2}{\gamma-1}c_\infty, \quad R_i = V_{ni} + \frac{2}{\gamma-1}c_i$$

where $V_{n_\infty} = \vec{V}_\infty \cdot \hat{n}$, and $V_{n_i} = \vec{V}_i \cdot \hat{n}$. The normal velocity and sound speed on the boundary face of cell i are then given by:

$$V_n = \frac{1}{2}(R_i + R_\infty), \quad c = \frac{\gamma-1}{4}(R_i - R_\infty).$$

At an outflow boundary, the interior cell density and pressure along with the velocity are used to find the flow variables in the ghost cell:

$$\rho = (\rho_i^\gamma c^2/p_i\gamma)^{1/(\gamma-1)}, \quad \vec{V} = \vec{V}_i + (V_n - V_{n_i})\hat{n}.$$

Similarly, at an inflow boundary, the free stream density, pressure and velocity are used to calculate the flow variables in the ghost

$$\rho = (\rho_\infty^\gamma c^2/p_\infty\gamma)^{1/(\gamma-1)}, \quad \vec{V} = \vec{V}_\infty + (V_n - V_{n_\infty})\hat{n}.$$

In both cases the pressure is found using the relation $p = \rho c^2/\gamma$. In the above equations γ is the ratio of specific heats.

A more rigorous set of far-field boundary conditions is based on the B_1 operator of Bayliss and Turkel [6], [7]. They assumed that the solution in the far-field has a wave-like behavior and then constructed a set of far-field boundary condition operators using asymptotic expansions. Similar boundary conditions were also given by

Tam [13]. The B_1 operator satisfies the equality for the asymptotic approximation to $O(r^{-3})|_{r=r_b}$, where r_b is the position of the boundary point from an interior reference point. This operator is basically given by

$$B_1 = \frac{\partial}{\partial \tau} + \frac{\partial}{\partial r} + \frac{1}{r}$$

where

$$\tau = \beta c_\infty t + \beta^{-1} M_\infty x, \quad r^2 = \beta^{-2} x^2 + y^2 + z^2, \quad \text{and}$$

$$\beta^2 = 1 - M_\infty^2.$$

At a subsonic inflow boundary the only characteristic that is out-going is associated with the acoustic waves, and therefore, the following radiation boundary conditions are applied:

$$(\frac{\partial}{\partial \tau} + \frac{\partial}{\partial r} + \frac{1}{r}) \left\{ \begin{array}{c} \rho' \\ u' \\ v' \\ w' \\ p' \end{array} \right\} = 0.$$

At a subsonic outflow boundary, the characteristics that are out-going are associated with acoustic waves, entropy waves and vorticity waves. Therefore, at such boundaries, together with the linearized momentum equations the following equations are solved:

$$\frac{\partial \rho'}{\partial t} + u_\infty \frac{\partial \rho'}{\partial x} = \frac{1}{c_\infty^2}(\frac{\partial p'}{\partial t} + u_\infty \frac{\partial p'}{\partial x}),$$

$$(\frac{\partial}{\partial \tau} + \frac{\partial}{\partial r} + \frac{1}{r}) p' = 0$$

where τ and r are as defined above, and it has been assumed that the free stream velocity is aligned with the x-axis, and a prime refers to the deviation from the free stream value of the associated quantity.

In solving aeroacoustics problems accurate definitions of the solid wall boundary conditions are also important. In numerical algorithms that use finite volume techniques, the application of the solid boundary conditions are rather simpler, since the finite volume technique requires the fluxes across the cell faces. In the current method, ghost cells are used at the wall and the velocity components at the ghost cells are determined forcing a prescribed mass flux boundary condition. Then the density is solved from the mass conservation equation.

3 Kirchhoff Method

The generalized form of the Kirchhoff formula for moving and deforming surfaces was given by Farassat and Myers [5]. The current approach to the prediction of noise radiation from ducted fans is to use a Kirchhoff surface that is fixed relative to the source (in this case the engine inlet). Thus Farassat and Myers' general equation was reduced to [14]

$$4\pi p'(\vec{x},t) = \int\int_S [\frac{E_1}{r(1-M_r)}]_{\tau_C} dS + \int\int_S [\frac{p' E_2}{r^2(1-M_r)}]_{\tau_C} dS \qquad (7)$$

where

$$M_r = \vec{M} \cdot \frac{\vec{r}}{|\vec{r}|}$$

and

$$E_1 = -(\hat{n} \cdot \nabla p' + \frac{\vec{M} \cdot \hat{n}}{c_\infty} \frac{\partial p'}{\partial \tau}) + \frac{1}{c_\infty (1-M_r)} (\cos\theta - \vec{M} \cdot \hat{n})(c_\infty \vec{M} \cdot \nabla p' + \frac{\partial p'}{\partial \tau}),$$

$$E_2 = \frac{1-M^2}{(1-M_r)^2}(\cos\theta - \vec{M} \cdot \hat{n})$$

in which $\hat{n}$ is the normal vector pointing out of the control surface (Kirchhoff surface), p' is the acoustic pressure, $\vec{M}$ is the Mach number vector, $\vec{r}$ is distance vector connecting the control surface point C, $(\vec{y})$, to the observer point $(\vec{x})$, $(\vec{r} = \vec{x} - \vec{y})$, and θ is the angle between the vector $\vec{r}$ and the vector $\hat{n}$. The integrands of Equation (7) are to be evaluated at the control point emission time, τ_C.

The control surface is constructed out of the CFD grid by specifying constant ξ, η, and ζ grid lines. Since Equation (7) requires the surface parameters, such as the normal vector and surface element area, the finite volume grid of the Navier-Stokes method readily provide this information. The Kirchhoff surface must be selected such that on the surface all the acoustic phenomenon is linear since the derivation of the Kirchhoff method assumes linear acoustics [5]. Nonlinear effects are important in the near field and it is hoped that the Kirchhoff surface can be formed at several wavelength distance.

4 Results

The Navier-Stokes/Euler and the Kirchhoff methods have been both implemented on the connection machine, and tested for several cases. This section presents steady state results for a transonic airfoil, RAE 2822, and acoustic radiation from a moving and pulsating cylinder. The effect of the spatial discretization on the requirement of the number of cells per wave length is discussed taking a 1-D wave problem case. Also presented in this section are the test results of the Kirchhoff

method and the coupling results of the Euler/Kirchhoff methods for a stationary and pulsating sphere.

4.1 Steady flow over a transonic airfoil

Figure 4 shows the steady state pressure distribution on an RAE 2822 airfoil at a Mach number of 0.676 and angle of attack of 1.89 degrees using the grid system shown in Figure 5. The solid line indicates the inviscid solution and the symbols indicate the experimental data [15]. Overall comparison is good even though some differences are seen in the aft portion of the airfoil due to viscous effects.

4.2 Moving and pulsating cylinder

As an unsteady flow case, a cylinder of finite radius that is simultaneously moving and pulsating was chosen. The Euler equations were solved due to the nature of the test case selected. With this test it was hoped to observe a continuous acoustic radiation from the cylinder with a doppler effect, as well as how the far-field boundary conditions work against the continuous acoustic radiation. The grid used for this problem is shown in Figure 6. For test purposes the frequency was chosen low so that the the number of grid points required was low and so was the computation time. There were approximately 30 cells per wave length in the upstream direction, and there existed a higher number of cells per wave in the downstream direction due to the doppler effect. This case was performed by first obtaining the steady state flow field and then turning on the time accurate solid wall boundary conditions. The wall conditions in a finite volume technique is implemented conveniently only by defining the time dependent mass flux through the solid surface. In this test case the mass flux was defined as a sinusoidal function of time. The time history of the convergence to the steady state for this problem is shown in Figure 7. Figure 8 compares the pressure coefficient contours of the current solution to the linearized potential solution. The overall pattern of the contours looks good. Finally Figure 9 shows the acoustic wave pattern emanating from the moving and pulsating cylinder. Notice that there are no apparent reflections from the far field boundary indicating that the far field boundary conditions work very well. Also the frequency shift due to the motion of the cylinder is noticeable.

4.3 One-D wave

Figure 10 shows the results of a 1-D wave propagation given by the second order finite volume and the fourth order finite volume discretization with the exact wave propagation. The number of cells per wave length is 20. The second order result diverges from the analytical solution quickly while the higher order result starts deviating from the exact solution after several wave lengths. The second order accurate scheme required nearly 50 cells per wave length while the fourth order accurate scheme required 20 cells per wave length for the same order of error.

4.4 Coupling of the Kirchhoff and N-S codes

The Kirchhoff method has been tested for a moving point source at different speeds. For this case the exact solution is available, and can be found in Morse and Ingard [16]. For convenience the Kirchhoff surface was chosen as a cube and the surface elements were generated by dividing the faces of this cube into equal number of panels whose sizes are dictated by the frequency constraint. The acoustic pressure and its derivatives on the Kirchhoff surface were obtained using the expression for the exact solution so that a direct comparison with the exact solution was possible. Having computed the acoustic pressure and its derivatives on the Kirchhoff surface Equation (7) was simply integrated assuming that the pressure and its derivatives on each element of the surface were constant, provided that the elements were sufficiently small. The results from one case is given here, Figure 11. For this case the Mach number is (0.5,0,0) and the frequency of the source is $10KHz$. For convenience the Kirchhoff surface was chosen as a cube and the faces of this cube were decomposed into equal sized panels, such that there existed approximately 63 points per wave length. The observer was located at (2500,0,500) meters, and the start of the observation time is 10 seconds, but shown as zero in the figure. The direction of the source movement was chosen such that it does not lie in the observer position direction, providing an asymmetry to the problem. The Kirchhoff results compare perfectly to the analytical solution, and this was always the case for other frequencies and speeds.

The Kirchhoff method has been implemented on the Connection Machine computer using Fortran 90. The Kirchhoff formula alone is well suited to massively parallel computers since it involves essentially zero interprocessor communication. So the above test cases performed quite well on the Connection Machine computers. One of the test cases used 240,000 elements on the Kirchhoff surface. On a 2048 processor CM-200 (i.e. 64 weitek floating point chips), the code achieved 150 megaflops. On a 32 node CM-5, it achieved 1,400 megaflops. So the CM-200 and CM-5 computers achieved 12 and 34 percent of their peak speeds respectively. When coupled to the Navier-Stokes code, the only requirement of the Kirchhoff code for communi-

cation is due to the necessary interpolation procedure. The coupling is described below.

The Kirchhoff method and the Navier-Stokes/Euler method have been coupled to each other and tested for a stationary pulsating sphere. The coupling is realized through a time marching and interpolation procedure. First, for a given observer position and time, the elapsed time for a disturbance to travel from its source to the observer is determined. The sources of the disturbances are the Kirchhoff surface elements and therefore each element has a different elapsed time, and correspondingly a different emission time. For a given observer time and position these different emission times form an emission time spectrum. This is schematically shown in Figure 12. On the Kirchhoff surface, the history of the acoustic pressure in this spectrum is required by the Kirchhoff formula. Also required in this spectrum are the position vectors of the surface elements. Since the emission time for a surface element can fall anywhere in the spectrum, an interpolation procedure is likely to get the accurate information since from the Navier-Stokes solver only certain discrete time step solutions are available. In aeroacoustic applications, e.g. radiation from a ducted fan, the observer (e.g. a microphone) and the source (Kirchhoff surface) are fixed relative to each other. Therefore, defining the observer position and the speed of the source as inputs make the predetermination of some of the parameters such as the minimum and maximum elapsed times, consequently the length of the emission time spectrum, possible. These parameters are calculated within a preprocessing routine. Other calculations such as the interpolations and integrations are done during the Runge-Kutta time stepping. This coupling is schematically illustrated in Figure 13.

This coupling was tested using a stationary pulsating sphere for which an analytical solution is available [17]. A constant k plane of the grid system used for this problem is shown in Figure 14. For comparison purposes two different Kirchhoff surfaces were constructed out of the grid system. The first Kirchhoff surface was the constant $j = 11$-surface, and the second surface was the constant $j = 21$-surface. Since the previous tests of the Kirchhoff method gave perfect results, any phase and amplitude error accumulations would show up by just comparing the solutions given by the two surfaces. The acoustic excitation was created by defining a time dependent mass flux across the surface of the sphere: $\rho v_n/\rho_0 c_0 = 0.005\sin(\omega t)$. The full nonlinear Euler equations were solved. The amplitude of the mass flux was chosen low just to have the nonlinear terms negligible. The frequency of the source was $500Hz$. The observer location was (20,10,0) meters from the center of the sphere. The results of the coupling are shown together with the analytical solution in Figure 15. The Euler solver was second order accurate in space. Although the observation period is short, this figure shows the phase errors due to the Euler solver.

5 Conclusions

This paper describes a hybrid approach, where a finite volume Navier-Stokes/Euler code has been coupled to a Kirchhoff code. This code is being modified to model engine inlet type geometries like the JT15D turbofan engine inlet which has been tested both experimentally and numerically [3], [18]. The boundary conditions of Bayliss and Turkel have also been incorporated into this program, to minimize reflections from the outer boundary.

This hybrid approach is very promising since it will reduce the demands on the Navier-Stokes solver. The Navier-Stokes solver will only be used in the near-field where it is essential. In the region where linear acoustics applies, it is much more efficient to use the Kirchhoff formula.

Acknowledgements

The authors gratefully acknowledge support from NASA Langley Research Center Grant Number NAG-1-1367.

References

[1] Eversman, W.; "Theoretical Models for Duct Acoustic Propagation and Radiation," in Aeroacoustics of Flight Vehicles: Theory and Practice, Vol.2: Noise Control, NASA Reference Publication 1258, vol.2, August 1991.

[2] Tyler, J. M. and Sofrin, T. G.; "Axial Flow Compressor Noise Studies," SAE transactions, vol.70, 1962, pp.309-332.

[3] Eversman, W., Parret, A. V., Pressier, J. S., and Silcox, R. J.; "Contributions to the Finite Element Solution of the Fan Noise Radiation Problem," Transactions of the ASME, vol. 107, April 1985.

[4] Jaeger, S. M. and Korkan, K. D.; "On the Prediction of Far Field Computational Aeroacoustics of ADV Advanced Propellers," AIAA Paper 90-3996, 1990.

[5] Farassat, F. and Myers, M. K.; "Extension of Kirchhoff's Formula to Radiation from Moving Surfaces," Jnl. of Sound and Vib., Vol. 123, No. 3, 1988, pp. 451-460.

[6] Bayliss, A. and Turkel, E.; "Radiation Boundary Conditions for Wave-Like Equations," Comm. on Pure and Appl. Math., Vol. 33, 1980, pp. 707-725.

[7] Bayliss, A. and Turkel, E.; "Far Field Boundary Conditions for Compressible Flow," Jnl. of Comp. Physics," Vol. 48, 1982, pp. 182-199.

[8] Long, L. N.; "A 3-D Compressible Navier-Stokes Code using Parallel Fortran," AIAA 10th Computational Fluid Dynamics Conference, AIAA CP-914, Honolulu, Hawaii, June, 24-27, 1991.

[9] Long, L. N., Khan, M. M. S., and Sharp, H. T.; "Massively Parallel Three-Dimensional Euler/Navier-Stokes Method," AIAA Jnl., vol. 29, no. 5, May 1991, pp. 657-666.

[10] Jameson, A., Schmidt, W., and Turkel, E.; "Numerical Solutions of the Euler Equations by Finite Volume Methods Using Runge-Kutta Time-Stepping Schemes," AIAA Paper 81-1259, June 1981.

[11] Rai, M. M., and Chakravarty, S.; "Conservative High-Order-Accurate Finite-Difference Methods," AIAA 93-3380-CP, 11th AIAA Computational Fluid Dynamics Conference, July 6-9, 1993.

[12] Harten, A., and Chakravarty, S. R.; "Multi-Dimensional ENO Schemes for General Geometries," NASA Contractor Report No. 187637, NASA Langley Research Center, September 1991.

[13] Tam, C. K. W. and Webb, J. C.; "Dispersion-Relation-Preserving Finite Difference Schemes for Computational Acoustics," to be appear in Journal of Computational Physics, 1993.

[14] Ozyoruk, Y. and Long, L. N.; "A Hybrid Scheme for Noise Radiation From Ducted Fans," Proceedings of NOISE-CON 93, Noise Control in Aeroacoustics, ed. H. H. Hubbard, May 1993, pp. 577-582.

[15] Cook, P. H., McDonald, M. A., and Firmin, F. C. P.; "Airfoil RAE 2822 Pressure Distribution and Boundary Layer Measurements," AGARD AR 138, 1979.

[16] Morse, P. M. and Ingard, K. U.; Theoretical Acoustics, McGraw-Hill, 1968.

[17] Peirce, A. D.; Acoustics, *An Introduction to Its Physical Principles and Applications*, Acoustical Society of America, 1989.

[18] Pressier, J. S., Silcox, R. J., Eversman, W., and Parret, A. V.; "A Flight Study of Tone Radiation Patterns Generated by Inlet Rods in a Small Turbofan Engine," 1984 AIAA Paper 84-0499.

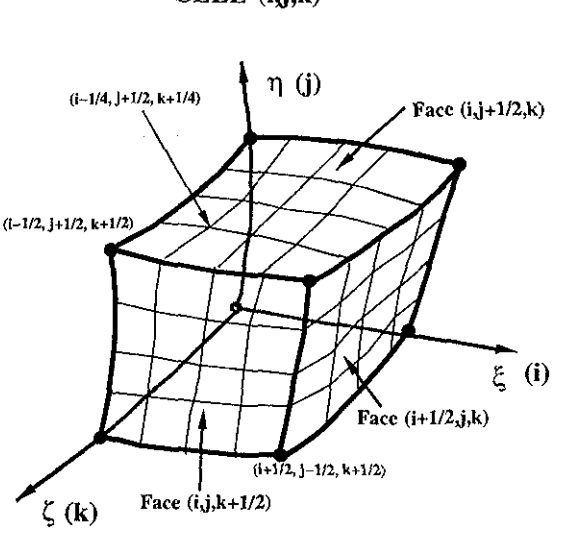

Figure 1: A computational cell.

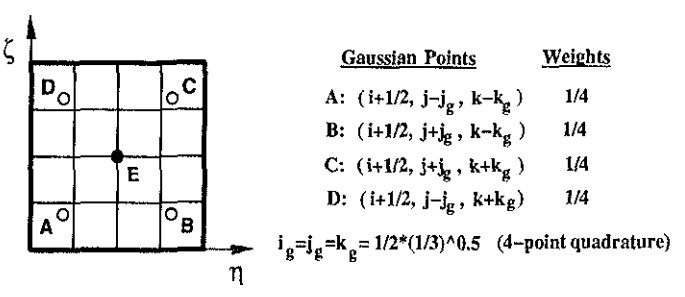

Figure 2: Constant ξ-face and Gaussian points.

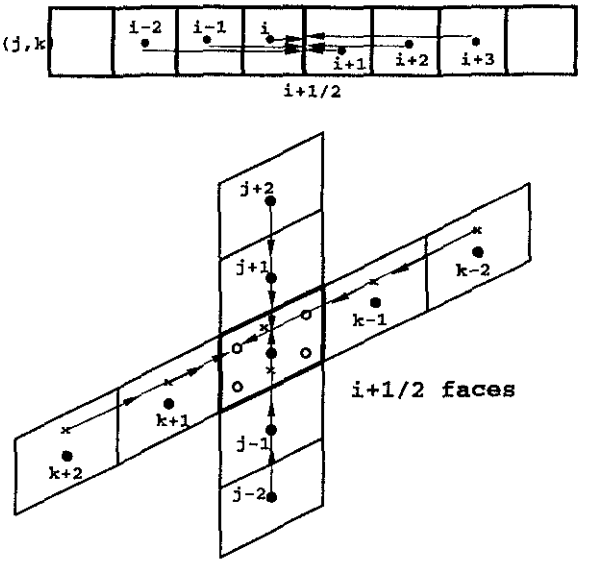

Figure 3: Interpolation for a Gaussian point.

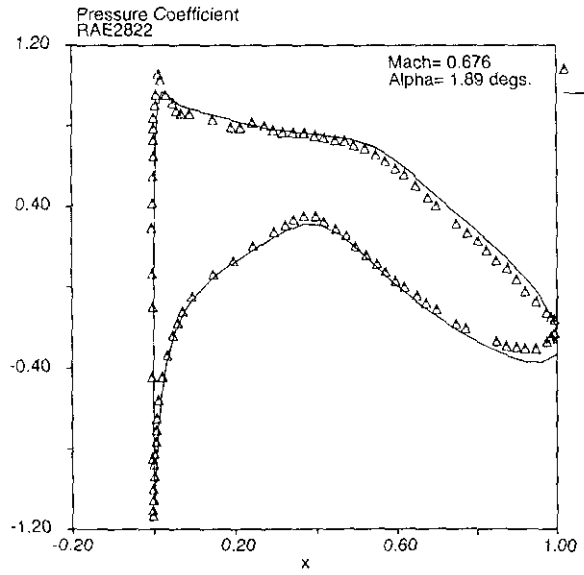

Figure 4: Pressure coefficient distribution on a RAE 2822 airfoil at $M = 0.676, \alpha = 1.89°$.

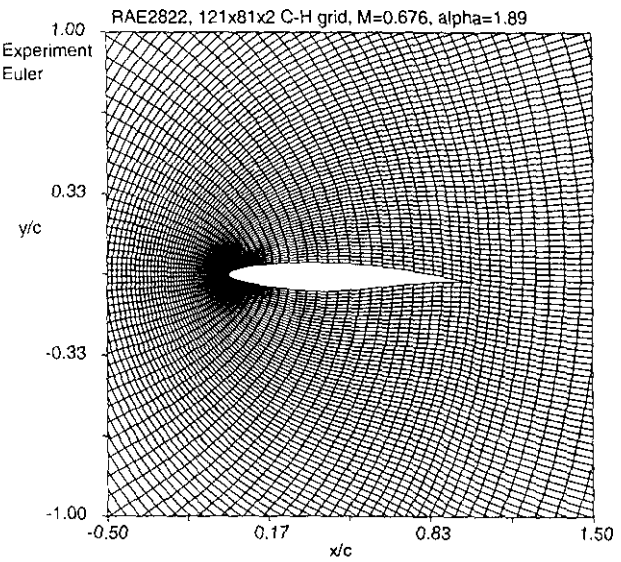

Figure 5: Partial view of the 121x81 grid system for a RAE 2822 airfoil.

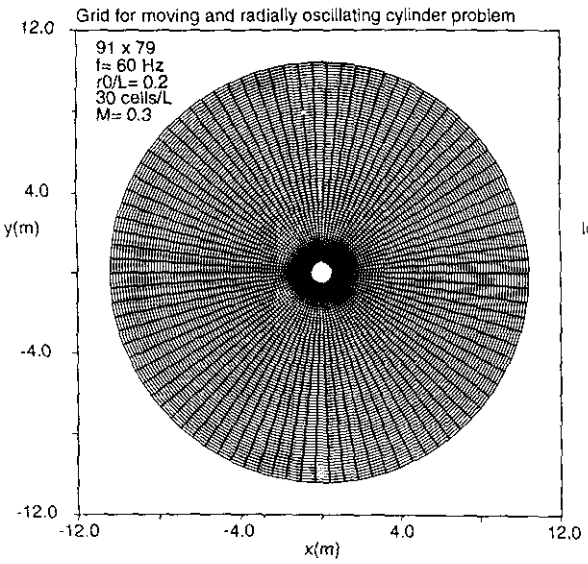

Figure 6: The 91x79 grid system for moving and pulsating cylinder.

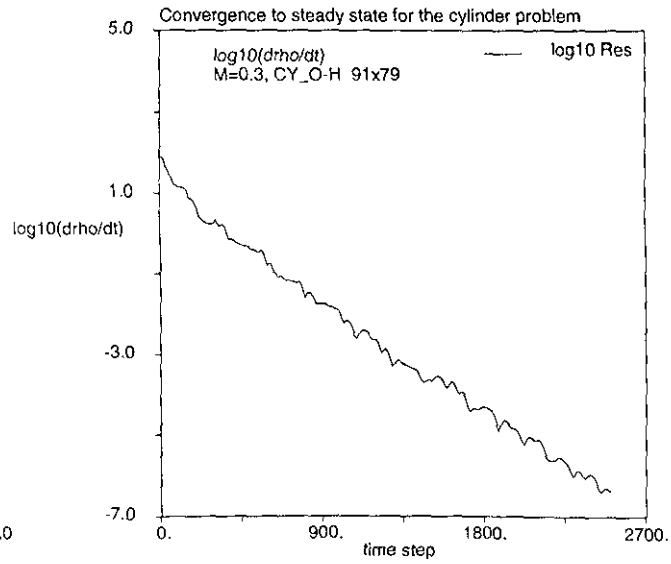

Figure 7: Convergence to steady state.

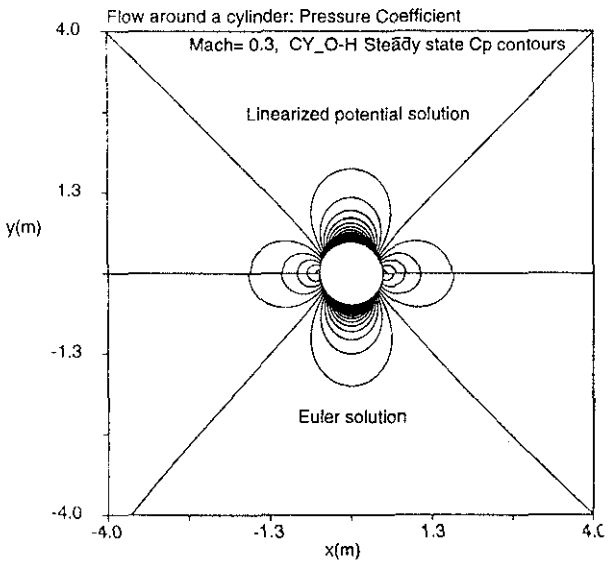

Figure 8: Pressure coefficient contour around a cylinder. Comparison of Euler solution to linearized solution, $M = 0.3$.

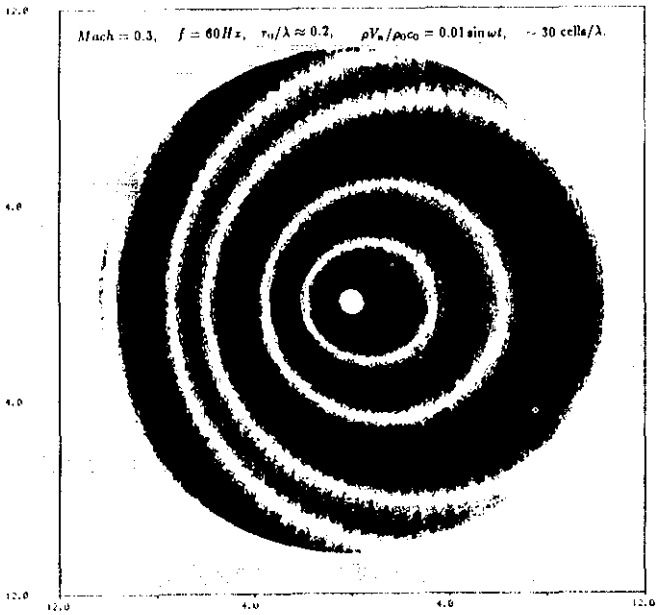

Figure 9: Acoustic pressure contours radiating from a pulsating cylinder at $M = 0.3, f = 60Hz, time = 0.098sec.$

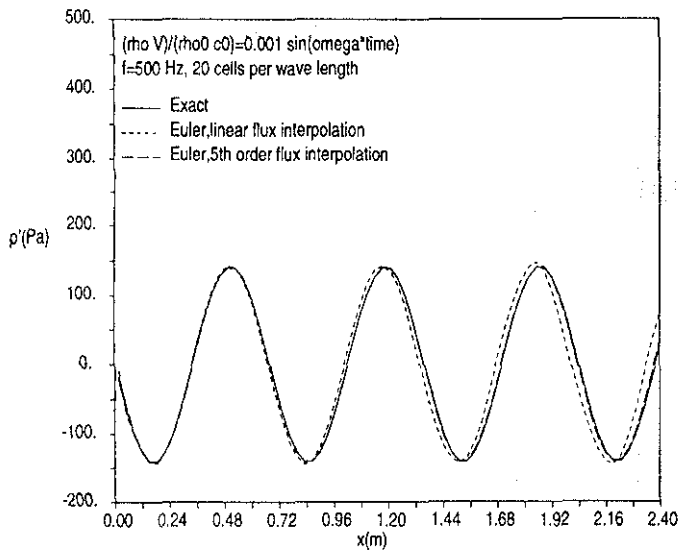

Figure 10: One dimensional wave propagation.

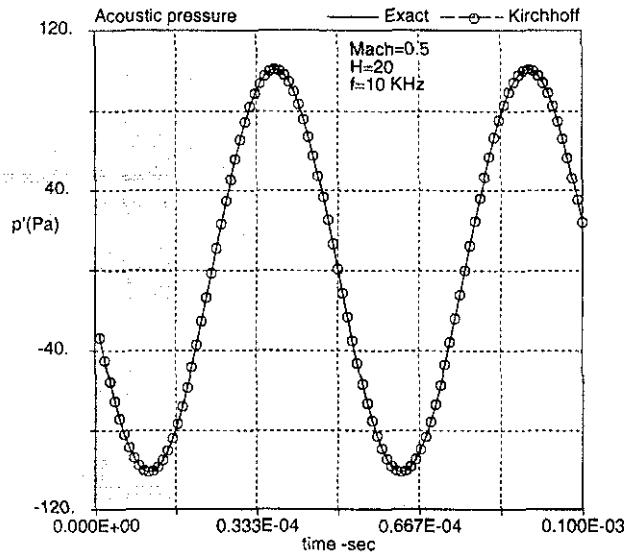

Figure 11: Sound radiation from a moving monopole. Kirchhoff result and the exact solution, $M = 0.5, H = 20, f = 10KHz$.

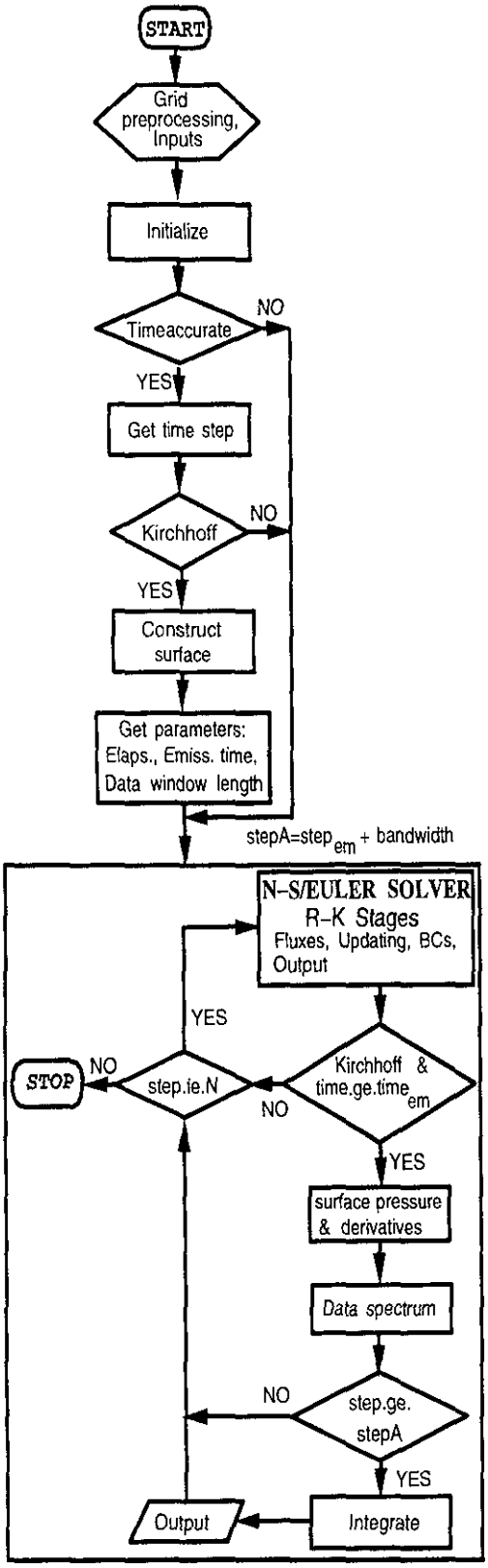

Figure 13: Coupling of N-S and Kirchhoff methods.

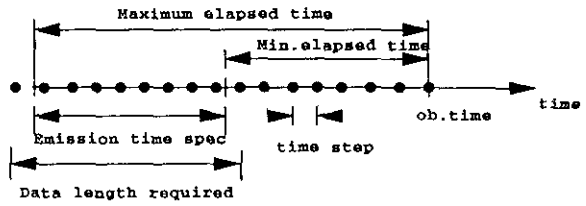

Figure 12: Emission time spectrum.

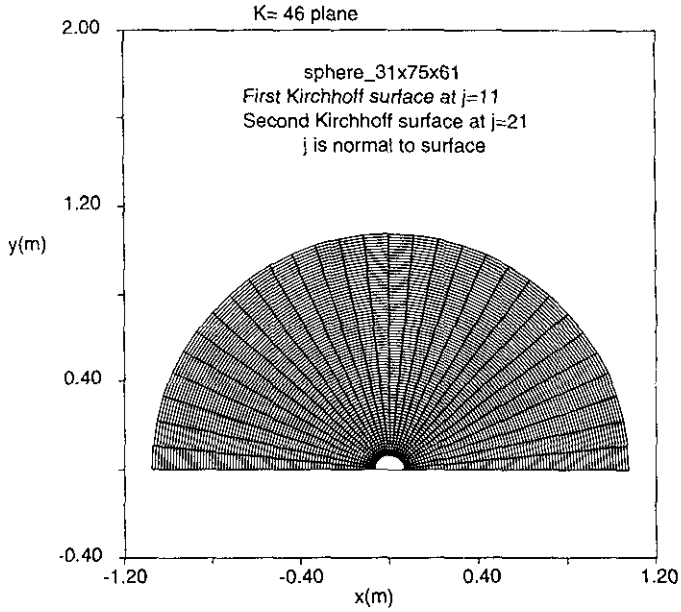

Figure 14: Spherical grid of N-S/Kirchhoff coupling problem.

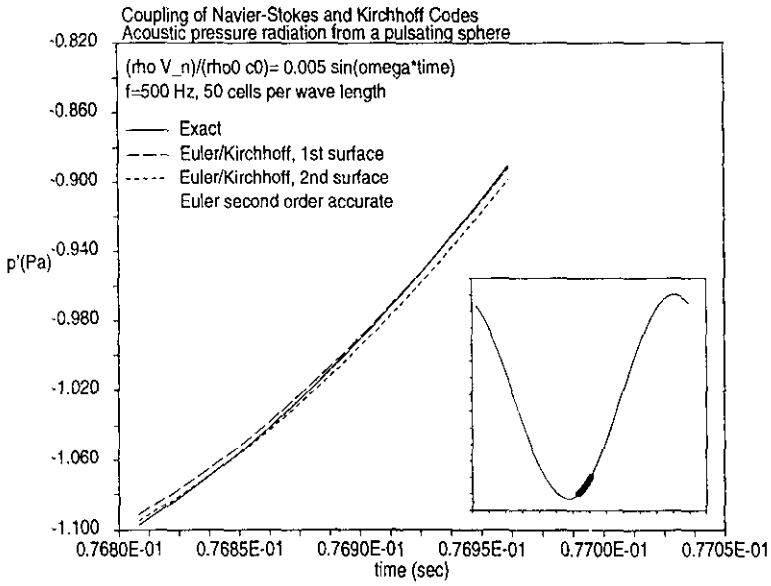

Figure 15: Sound radiation from a stationary, pulsating sphere.